UV line beam for display manufacturing

Andreas Heimes[a], Martin Wimmer[a], Torsten Beck[a], Christian Stolzenburg[b], Julian Hellstern[b], Christoph Tillkorn[b], Sören Richter[a], Thomas Zeller[a]

[a]TRUMPF Laser- und Systemtechnik GmbH, Johann-Maus-Str.2, 71254 Ditzingen, Germany;
[b]TRUMPF Laser GmbH, Aichhalder Straße 39, 78713 Schramberg, Germany;

ABSTRACT

UV line beam optics are nowadays an integral part of manufacturing chains in semiconductor and display technology. Amongst others the most prominent applications are the large area annealing of semiconductor materials and the laser lift off process used e.g. for debonding of flexible displays. Here we report on a very flexible platform based on our DPSSL technology and a wavelength of 343 nm. This laser technology provides superior reliability combined with very high pulse energy stabilities. Within our optical design the beam shape along the scan direction can be either gaussian or tophat. We show which fluences can be achieved depending on beam shape and beam width and refer to the relevant applications.

1. INTRODUCTION

Nowadays UV excimer lasers are a well established and well proven laser source when it comes to large area processing in micro-electronic manufacturing. With wavelengths ranging from 190 nm to 310 nm a large variety of applications can be addressed, like e.g. the laser annealing and doping of semiconductors or the ablation of plastic. The most prominent applications in the field of flat panel display (FPD) manufacturing are the production of low temperature polysilicon (LTPS) and the laser lift-off (LLO) associated with the debonding of flexible displays.

Up to now excimer line-beam optics with a beam-profile of typically $\sim 500\,\mu$m width and line-lengths up to 1500 mm have established as the current standard used in mass production systems.[1–3] Nevertheless, there are a few disadvantages associated with the excimer technology: Constant maintenance and commissioning make these systems very expensive in the long run. Due to limited pulse repetition rate the productivity cannot be increased without decreasing the spatial pulse to pulse overlap. Line-beam systems that are based on diode pumped solid state lasers (DPSSL) are a promising alternative to the traditionally used excimer platforms. They offer lower maintenance and more ways to scale productivity.

Here we report on our DPSSL technology with a wavelength of 343 nm. We discuss the beam shaping techniques, which are associated with the DPSSL beam sources and are necessary to assure appropriate line-beam specifications. On the process side we focus on the laser-lift off (LLO) of polyimide (PI) and the laser annealing of silicon (LTPS). The potential advantages of the DPSSL platform in terms of quality and process margin are highlighted in this respect.

Further author information: andreas.heimes@trumpf.com

Proc. SPIE 11989, Laser-based Micro- and Nanoprocessing XVI, 119890J (4 March 2022), edited by Akira Watanabe and Rainer Kling; https://doi.org/10.1117/12.2608238

2. DPSSL-LINE BEAM SYSTEM

In this section the optical concept is discussed to create a line beam profile from several initially roundly shaped laser beams. In the following, we speak of the long axis when we mean the direction of the greatest expansion, and of the short axis when we refer to the expansion perpendicular to it. In Fig. 1 the individual building blocks are shown which are part of our line beam systems. This figure shows an exemplary optical setup, which illustrates the basic ideas, however, does not capture the details of the optical design our line beam systems are based on. We focus on the *laser source*, the necessary *beam shaping*, discuss different settings in terms of process *energy density* and take a look at an exemplary *line beam system*.

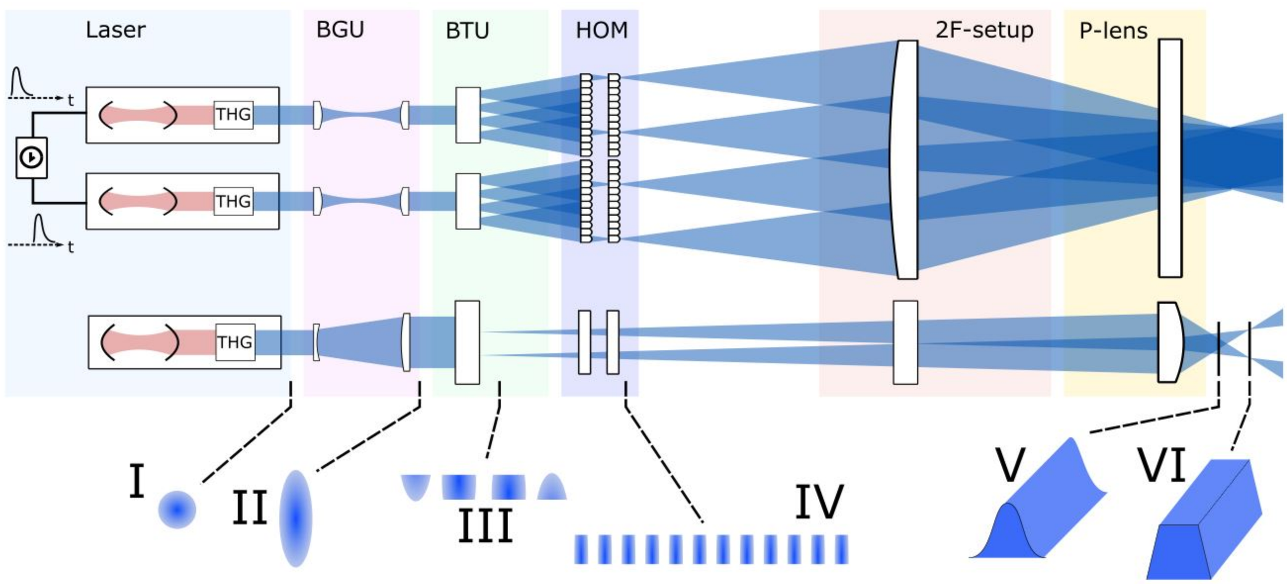

Figure 1. *Beam-Shaping Concept* - Long axis beam shaping (top), Short axis beam shaping (bottom): An initially roundly shaped beam I is emitted from a Laser source, consiting of an infrared resonator and a third harmonic generation (THG). A beam guiding unit (BGU) shapes the beam I into an elliptical beam II. The latter enters a beam transformation unit (BTU). The output beam III consists of severeal beamlets, which illuminate an imaging homogenizer (HOM). The output packages IV are integrated by a 2f-setup and superimposed in the working plane. A projection lens (p-lens) focuses/images the output of the BTU into working plane, yielding a gaussian (V) and tophat (VI) line beam profile.

Solid state laser - Our beam source is based on our TruMicro 8000 platform, providing superior reliability and low maintenance costs combined with very high pulse energy stabilities. The technology relies on a diode pumped, cavity dumped IR resonator, which emits pulses in the range of $\tau \sim 20\,\mathrm{ns}$ with a repetition rate of $f = 10\,\mathrm{kHz}$. Deviating frequencies or single shot operation are possible without changing the beam parameters. The third harmonic generation (THG) delivers a UV beam with a wavelength of $\lambda = 343\,\mathrm{nm}$, a beam quality of roughly $M^2 \sim 25$ and a pulse energy of about $E = 40\,\mathrm{mJ}$. A typical beam profile is depicted in Fig. 2a. The lasers are partially coherent sources, which are initially neither well suited for homogenization in the long axis nor for focusing in the short axis. In order to ensure this, however, specific *beam shaping* has to be applied, as discussed in the next paragraph. An arbitrary number of sources can be synchronized and electronically delayed, enabling arbitrary temporal pulse shaping. This is interesting because the temporal behaviour of the thermal load, depending on the particular process, can have a considerable influence on the process result. Within our technology individual time delays of up to 500 ns with a jitter to master clock $< 2\,\mathrm{ns}$ (1σ) are possible. As an example, in Fig. 2b-d, we compare a single pulse operation with a two hump temporal profile. In Fig. 2b four TruMicro 8340 with same energy level are synchronized to the same time delay of $dt_i = 0$. In Fig. 2c-d the lasers have individual time delays dt_i yielding a two hump profile.

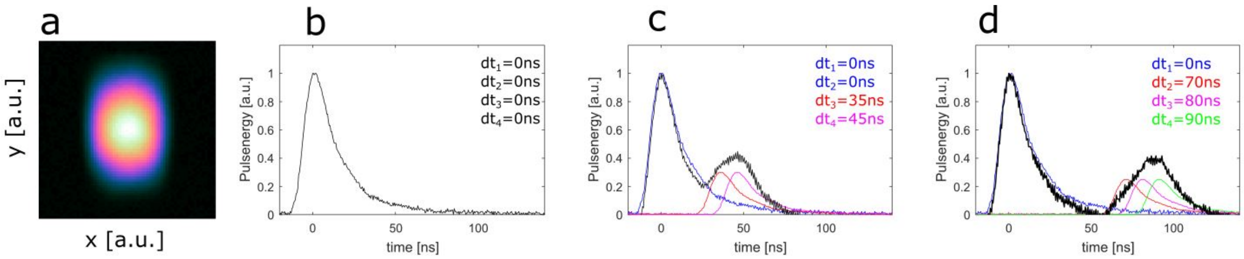

Figure 2. *Laser Source* - a. Typical gaussian-like profile of the TruMicro 8000 series. b-d Arbitrary pulse-shaping, realized by four synchronized laser sources, each with an individual time delay of dt_i, with $i = 1, 2, 3, 4$, and individual power setting.

Beam Shaping - The basic beam guiding and beam shaping concepts are shown in Fig. 1. One or several beams are guided to a beam transformation unit (BTU). The latter fulfills the purpose of manipulating the lateral beam coherence in the long and short axes in opposite directions. The beam quality along the long axis is degraded. This reduces interference effects, which might be caused by e.g. homogenizing techniques. In the short axis, there is an improvement in beam quality and thus better focusability. For a detailed discussion of a possible technical design as well as a theoretical description we refer to Ref.[4] The beam profile III in Fig. 1 shows an typical output of the beam transformation unit. An initially elliptical beam, with a defined ratio of beam qualities, i.e. $M_x^2/M_y^2 \sim 1$, is split into a number of beam-lets which are spatially reoriented such that an aspect ratio $M_x^2 \gg M_y^2$ is realized.

The beam path after the BTU can be separated into two parts: a long axis beam shaping and a short axis beam shaping (see Fig. 1 top/bottom respectively). In long axis the beam-lets overlap and smoothly illuminate an imaging homogenizer (HOM). The latter splits the beam into several beam-lets in long axis, which are integrated by a subsequent 2f-setup in a far field plane. The result is a homogeneous tophat shaped beam profile in long axis.

In short axis the beams pass through one or more lenses which comprise at least one projection optic which focuses or images the BTU output into the working plane: The short axis profile either is a gaussian or a tophat (see beam profiles V and VI in Fig. 1). In Fig. 3 we show respective measurements of the short axis profile.

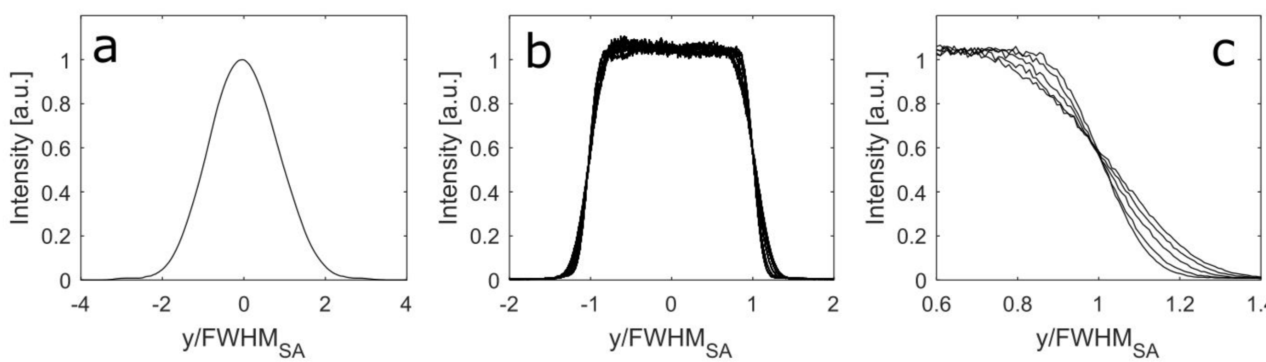

Figure 3. *Beam Profile* - Measurement of a short axis gaussian profile (a), several short axis tophat profiles with different steepness (b) and a close-up of the latter (c).

By manipulating the BTU output and/or by complementing additional lenses within the short axis beam path the short axis profile can be finely tuned with regard to beam shape, width and steepness. Fig. 3c shows that tophat steepness, e.g., can be finely tuned by manipulating the BTU output. In this way the beam shape can be changed such that it meets particular requirements of a process. In principle any beam shape in between gaussian and tophat can be realized.

Energy density - The maximum energy density F, as depicted in Fig. 4, depends on the number of lasers N within the system, their respective pulse energy E, the beam footprint defined by the full width half maximum in long axis and in short axis, i.e. $FWHM_{LA}$ and $FWHM_{SA}$, and the optics efficiency η, which among others accounts for transmission losses. For the maximum fluence for the tophat and gaussian profile we obtain

$$F_{tophat} = \frac{N \cdot E}{FWHM_{LA} \cdot FWHM_{SA}} \cdot \eta. \quad (1)$$

$$F_{gaussian} = \sqrt{\frac{4\,ln(2)}{\pi}} F_{tophat} = 0.94 \times F_{tophat} \quad (2)$$

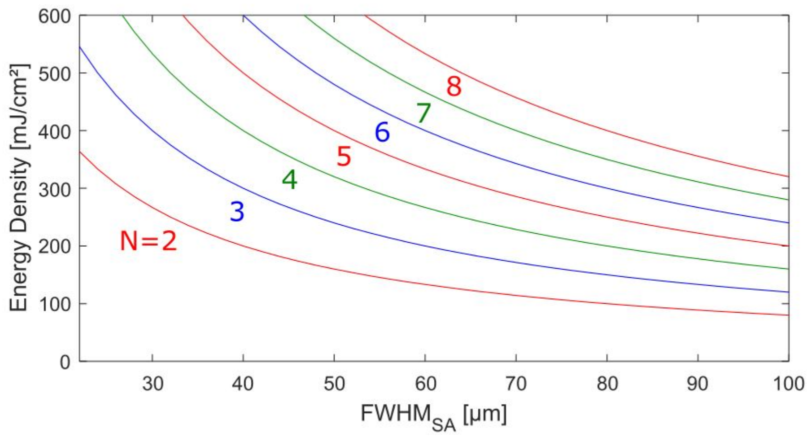

Figure 4. *Energy Density* - Energy density over short axis beam width as calculated by Eq. 1 for a line-length of $750mm$ and different numbers, N, of laser sources (TruMicro 8340).

Commonly one refers to the energy density, Eq. 1, when specifying an optical system, independent of whether the optical system hat a gaussian or tophat short axis profile. Eqs. 1 and 2 refer to the real physical maximum fluence, i.e. at same $FWHM_{SA}$ the maximum fluence of a tophat is slightly larger than that of the gaussian. In Fig. 4 the fluence, Eq. 1, is shown as a function of beam width for different number of laser sources and a fixed line-length of $FWHM_{LA} \approx 750\,\text{mm}$. An optics efficiency of $\eta = 75\,\%$ is used. A given fluence, defined by the underlying process, can be realized by either scaling the short axis beam width or adapting the number of laser sources. The productivity of a scanning process depends on both, the short axis beam width and the overlap of subsequent pulses. In the next sections we take a look at two important processes with in the display manufacturing chain, the laser lift off process and the laser annealing of Si-a. In this context we discuss the point of productivity again.

Optical system - As an example in Fig. 5 we show the drawing of our 750mm line beam system, which already was introduced in detail in Ref.[5] and consists of two TruMirco 8340, a beam guiding unit (BGU) and a line beam optics. This system has superior mechanical stability combined with a very small footprint. Within this setup a short axis profile, either gaussian or tophat, can be realized. The average intensity and short axis beam-width along long axis is shown in subpanel b. Beam-widths down to $25\,\mu\text{m} - 30\,\mu\text{m}$ are possible, depending on the beam shape. Furthermore the line length can be decreased. In this way fluences in the range of $300 - 600\,\text{mJ/cm}^2$ are possible. The statistical deviation along long axis is in the range $2\sigma_{LA} < 2.5\%$, whereas the homogeneity for the tophat in short axis is in the range $2\sigma_{SA} < 3.5\%$.

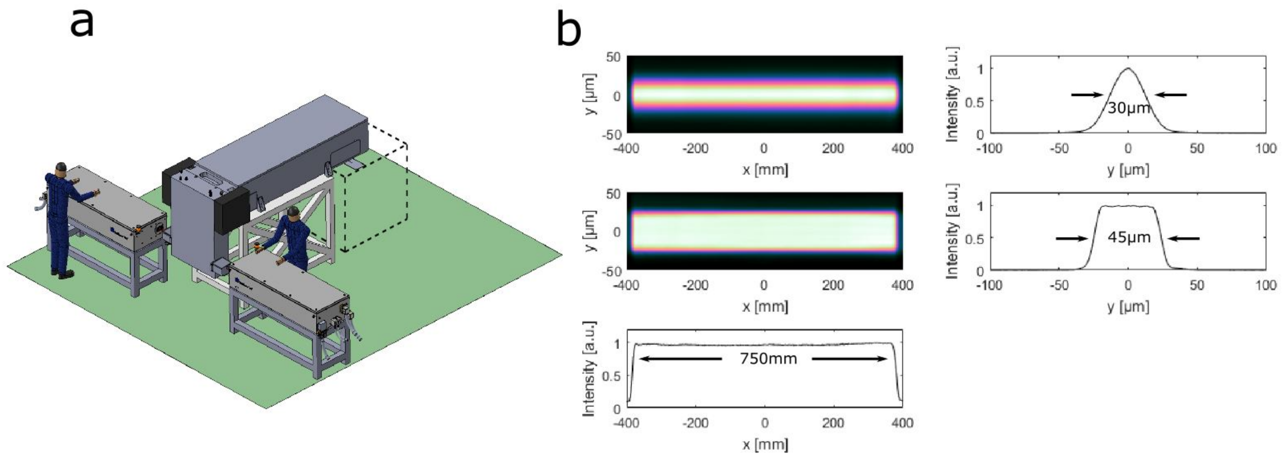

Figure 5. *Optical System* - a. Drawing of the *TRUMPF Line Focus System 750 UV* consisting of two laser sources (*TruMicro 8340*), a beam guiding unit and a line beam optics, combining four input beams into one line beam profile. b. Beam profiles which, among others, can be realized within the setup: a gaussian line beam profile with 30 μm width (top) and a tophat line beam profile with a width of 45 μm. A long axis cut is shown at the bottom. The measurements were done at maximum fluence level.

Finally, in Fig. 6, we show a collection of beam shapes that can be realized using our beam shaping technique. Panel (a) shows a beam profile with 75 μm in width and 1500 mm in length. This beam profile was realized using twelve *TruMicro 8340*. The measurement was performed at 100% laser power in working plane yielding a maximum fluence, Eq. 1, over 300 mJ/cm^2. Apart from continuous line beam shaped beam profiles other beam profiles can be realized by standard homogenization techniques. In Fig. 6b we show an intermediate image plane which can be used for mask projection. This system is operated with one *TruMicro 8340* yielding a substrate field size of about 1×1 mm^2 and a fluence up to 5 J/cm^2. This makes it a potential platform for lab applications or to address processes that require higher intensity.[6–9] Furthermore, in Fig. 6c, we show a line beam profile consisting of multiple square shaped spots with an individual size of $\sim 100\,\mu$m. This beam profile can be used for selective laser processing such as, e.g. the pixel separated laser induced forward transfer (LIFT) of micron size electronic devices such as μLEDs.

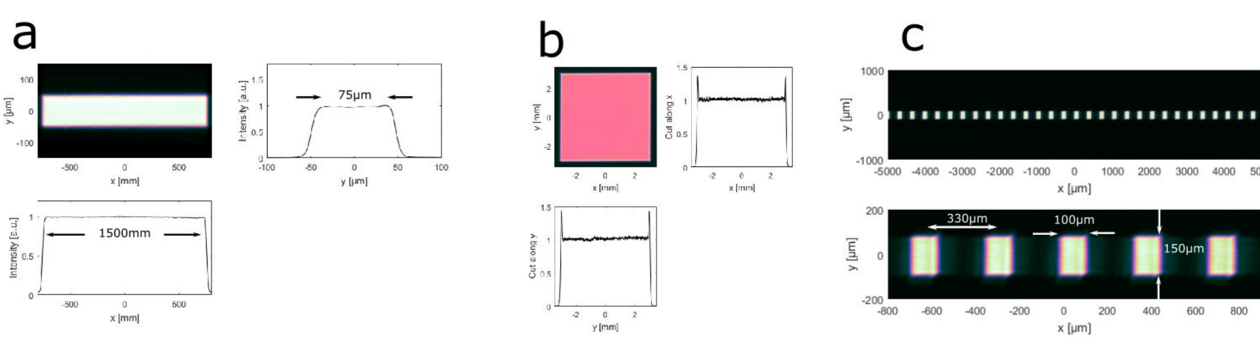

Figure 6. *Beam Shapes* - a. Measurement of a 1500 mm line beam with a short axis width of 75 μm. The measurement was performed using twelve synchronized laser sources (*TruMicro 8340*) at maximum laser power. b. 2D mask plane and corresponding cross sections of our optical system with $\sim 1 \times 1$ mm^2 substrate field size and a maximum fluence of 5 J/cm^2 using one *TruMicro 8340*. c. Homogenized spot-profile using high power capable beam-splitting techniques.

3. LASER LIFT OFF

There are various debonding processes using UV ns lasers and homogenizing optics. Here, a substrate is detached from a carrier material via laser ablation. One widely industrialized process in the field of solid state lasers is the debonding of flexible plastic films from glass substrates, used for the fabrication of flexible displays.[1,3] For laser lift-off (LLO) of flexible polyimides (PI) from a glass substrate, wavelengths from 248 nm to 355 nm are usually used. During laser treatment the PI is heated just above the ablation threshold. Usually this happens in the temperature range $T_C \sim 400 - 500\,^\circ$C.[1,3] Alternatively the PI film can have a thin *sacrificial layer*, e.g. ~ 50 nm amorphous silicon which acts as an absorption layer. In this section we will discuss the ablation of *pure* PI without sacrificial layer using two different types of short axis profiles. DPSSL Line beam systems with a gaussian short axis profile are widely used. In this section we highlight the advantages of using a tophat short axis profile.

Energy density and overlap - The absorption length $1/\alpha_{PI}$ of PI is much larger than the corresponding heat diffusion length $\xi \sim \sqrt{D\tau}$, where $D = \kappa_{PI}/\rho_{PI}C_{PI}$ is the heat diffusion coefficient and κ_{PI} and C_{PI} are the heat conductivity and the specific heat respectively. In this regime the thermal load within the PI occurs on the length scale of the absorption length. At an appropriate laser fluence ablation occurs within the penetration depth

$$z = \frac{1}{\alpha_{PI}} \ln\left(\frac{F}{F_C}\right), \qquad \text{with } F > F_C. \tag{3}$$

Here F_C is the ablation threshold energy density, which further depends on the reflectivity of the carrier glas and of PI, i.e. R_{glass} and R_{PI}, and the material parameters density ρ_{PI} and heat capacity C_{PI},

$$F_C = \frac{1}{\alpha_{PI}} \frac{\rho_{PI} C_{PI} T_C}{(1 - R_{PI})(1 - R_{\text{glass}})}. \tag{4}$$

The LLO scanning process leads to a finite ablation depth, which is generally larger than Eq. 3. The latter depends on the combination of both, the overlap of successive pulses, i.e.

$$\text{overlap} = 1 - \frac{\Delta s}{FWHM_{SA}}, \tag{5}$$

and the maximum fluence F applied to the subtrate. Here Δs is the scanning pitch between two successive pulses. The scanning speed, which finally determines the productivity, is given by the product of scanning pitch and laser repition rate, i.e.

$$v = FWHM_{SA}\,(1 - \text{overlap})\, f. \tag{6}$$

In Fig. 7 we compare the two beam profiles, gaussian and tophat, in terms of ablation depth and pulse overlap. The threshold at which the LLO occurs is shown by the white line in Figs. 7a and 7d for the gaussian and tophat profile respectively. The crosses in this figures indicate two situations: For a gaussian with overlap of 50% and a energy density $F_{max} = 1.4F_C$ the mean ablation depth is approximately 250 nm (see Figs. 7a-c). For the tophat profile lift off occurs already at smaller overlap and smaller ratio F_{max}/F_C (see Fig. 7d). In Figs. 7e and 7f we show the pulse to pulse scan and the ablation depth respectively. We find that less ablation depth and therefore ash production can be achieved, because the maximum energy density F_{max} is only slightly larger than F_C, corresponding to a small penetration depth, Eq. 3.

As an example we consider the 750 mm line beam system discussed in section 2. A gaussian with 30 μm width leads to a scanning speed of 150 mm/s at 50% overlap. The tophat profile with 45 μm width corresponds

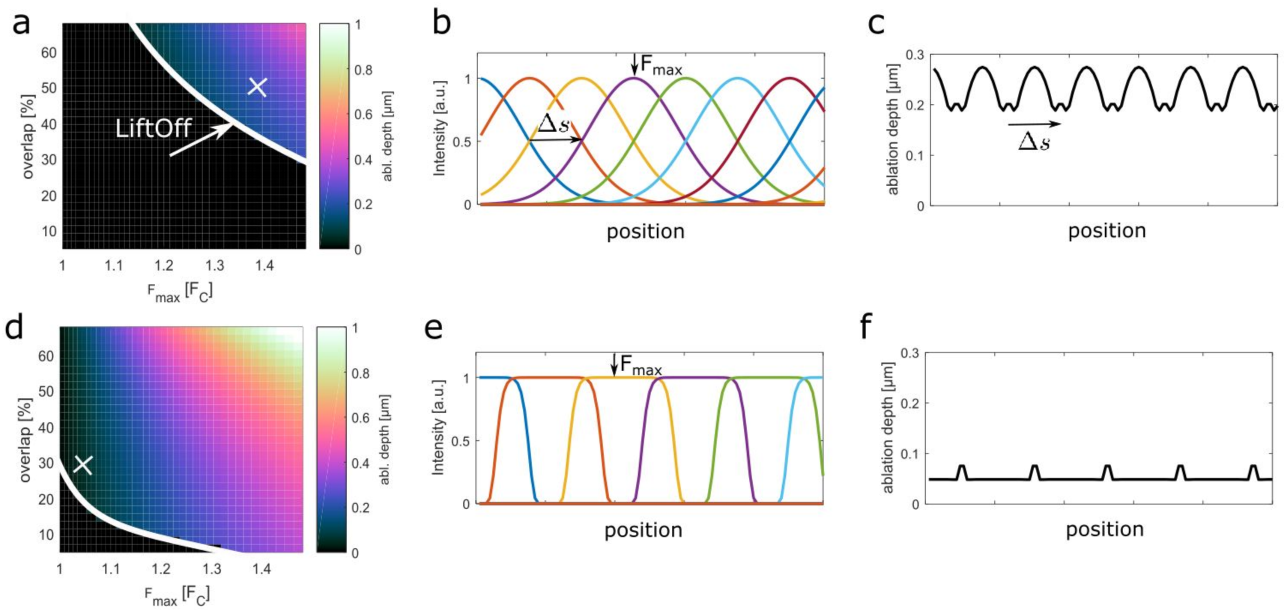

Figure 7. *Laser Lift Off* - a. Mean ablation depth as a function of overlap, Eq. 5, and energy density for the gaussian profile. b. Gaussian profiles with an overlap of 50%. c. Ablation depth over scanning direction for the cross indicated in panel (a). (d-f) The same as shown in (a-c) but for the tophat profile.

to a scanning speed of $v = 315\,\mathrm{mm/s}$ at 30% overlap. Mind that for this example the relative energy density per line length $F_{max}/F_C \times FWHM_{SA}$ for the gaussian and tophat is nearly the same. This means that for the $30\,\mu$m gaussian and the $45\,\mu$m tophat liftoff occurs at similar laser power. We find that in this sense, a tophat profile shows its advantages over the gaussian profile by its higher productivity and the potentially lower ash production.

4. SOLID STATE LASER ANNEALING

Compared to other backplane technologies such as amorphous silicon (Si-a) or oxides such as Indium-Gallium-Zink-Oxid (IGZO) the production polycrystalline silicon (LTPS), up to now, is very expensive. This is also due to reasons mentioned in the introduction. However, the LTPS technology has the technical advantage of high electron mobility and CMOS capability.[10] Accordingly, it would be desirable to gain a cost advantage in the LTPS technology. In this section we discuss the laser annealing process in the context of the solid state lasers and work out why this technology could bring an advantage.

Solid state laser annealing (SLA) of amorphous silicon (Si-a) to polycrystalline silicon (Si-p) follows the well-known excimer laser annealing (ELA) process, known from excimer line beam optics. Typically 50 nm thin amorphous silicon is coated on top of a glass or a flexible substrate and rapidly heated by ns UV laser pulses. The pulse energy is chosen such that the silicon is nearly completely melted, leaving single localized seeds. The latter serve as nuclei for lateral crystal growth. This situation is shown in Fig. 8. The process result and associated parameters like grain size, grain periodicity and surface roughness critically depend on the laser parameters energy density, polarization and temporal pulse shape. The DPSSL technology offers possibilities to easily manipulate these laser parameters and thus optimize the process result.

Energy density - The energy density needed to locally enforce a near complete melting, crucially depends on how much energy is deposited in what period of time. Considering the oversimplified example of an rectangular temporal pulse shape the threshold energy density needed to reach the melt temperature T_m can be estimated by[11]

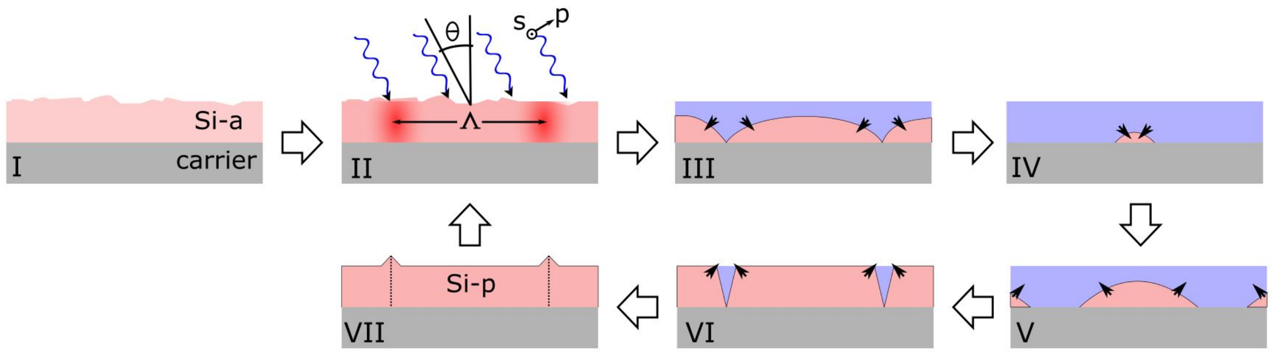

Figure 8. *Solid State Laser Annealing* - Initially amorphous silicon (I) is heated by laser irradiation. The interaction of the light with a given but arbitrary surface roughness leads to a periodic heat input on the length scale Λ (II). Melting occurs (III) and leaves localized seeds (IV) which grow during cool down (V). Protrusions occur at the grain boundaries as they form (VI). Here, the surface piles up due to the difference in density between liquid and solid silicon (VII). These periodic features reinforce the effect of the laser-induced periodic structure. The process of melting is repeated multiple times.

$$F = \frac{\rho C_p (T_m - T_0)\sqrt{\pi D \tau}}{2(1-R)} \tag{7}$$

Here ρ and C_p are the density and the specific heat capacity, $D = \kappa/\rho C_p$ is the heat diffusion constant, where κ refers to the thermal conductivity. Furthermore T_0 is the ambient temperature and R is the reflectivity of silicon. Eq. 7 implies that the application of energy within a shorter period of time results in an effectively smaller energy density. Using the material parameters mentioned in Ref.,[11] for amorphous and crystalline silicon respectively, and the pulse duration discussed in sec.2, we obtain

$$F(\lambda = 343nm, \tau = 20ns) \approx 280 \frac{\mathrm{mJ}}{\mathrm{cm}^2} \tag{8}$$

for threshold energy density to melt crystalline silicon. For typical excimer parameters we obtain $F(\lambda = 308nm, \tau = 30ns) \approx 370 \frac{\mathrm{mJ}}{\mathrm{cm}^2}$. This is consistent with results in Refs.[12,13] The respective process energy density, which is defined by the optimal process result, will be in the order of Eq. 8. Thus, this simple example already gives a good estimation on the process parameter energy density. It shows that short pulse duration may be beneficial in terms of lower energy density.

Polarization - Within a particular and narrow energy window close to Eq. 8 the grains order in a periodic fashion. This is a consequence of laser-induced periodic surface roughness and a positive feedback effect due interference caused by this periodic pattern.[14–16] The result is an effectively periodic temperature pattern[12]

$$T(r_\perp) = T(0)[1 + \alpha(k_\Lambda) sin(k_\Lambda \cdot r_t)], \tag{9}$$

where $r_\perp$ is the lateral spatial coordinate and $k_\Lambda = 2\pi/\Lambda$ is the spatial frequency component corresponding to a surface roughness with periodicity Λ. Fig. 8 shows the one dimensional situation with light incident by an angle θ. Interaction with the surface roughness leads to a periodic temperature dependence which depends on the polarization state.[12] P-polarized light leads to a period $\Lambda \approx \lambda/[1 \pm sin(\theta)]$ and s-polarized light yields $\Lambda \approx \lambda$.[12,15,16] As depicted in Fig. 8 a periodic temperature distribution creates a periodic melting depth and therefore initiates the formation of periodically arranged seeds. The polarization has great impact on this order and consequently can be used to directly manipulate the grain distribution.

Temporal pulse shape - Another important factor is the temporal heat load during phase transitions from solid to liquid and reverse. The factor $\alpha(k_\Lambda)$ in Eq. 9, e.g., determines the shape of the remaining seeds: A small value corresponds to slowly varying temperature and therefore shallow grains, whereas a large value leads to more strongly localized grains. In the appendix A we show that the factor $\alpha(k_\Lambda)$ depends on the pulse duration τ, i.e.

$$\alpha(k_\Lambda) \propto \operatorname{erf}\left(\sqrt{D\tau} k_\Lambda\right)/\sqrt{D\tau} k_\Lambda. \tag{10}$$

The functional dependence is a consequence of lateral heat distribution. During the time period τ heat is distributed over a length scale $\xi = \sqrt{D\tau}$. A short pulse duration leads to strongly localized heat accumulation within the range of the grain size, i.e. $\xi(20\,\mathrm{ns}) \sim 370\,\mathrm{nm}$. This gives rise to the possibility of highly localized seeds. Long pulse duration leads to an decrease of the factor Eq. 10 and thus to a formation of shallow seeds. In this context pulse duration and pulse rise time may have a crucial influence on the polycrystalline grain distribution in terms of its periodicity. To be mentioned, that a short pulse duration also leads to rapid cooling. This can cause amorphisation and may also affect the surface roughness. In order to circumvent this a secondary pulse becomes necessary which prevents the substrate from rapid cooling.[12,17]

As shown in Fig. 2 the DPSSL technology offers very flexible platform with comparatively short pulses and the ability to create an appropriate temporal pulse shape. The combination of multiple light sources, as discussed in section 2, opens new perspectives to finely control the process of melting and crystallization on a 100 ns scale and directly influence parameters like grain distribution and surface roughness. In this way the process margin can be enlarged.

Beam profile - The SLA process necessitates a homogeneous tophat profile in both, long and short axis. As discussed in section 2 this is possible within our DPSSL technology. In order to meet the required process energy density, the beam width can be choosen in the range of $30\,\mu$m to $100\,\mu$m, depending on the number of lasers (see Fig. 4). Productivity is ensured by the high repetion rate of the laser. For a beam profile with $45\,\mu$m width, as shown in Fig. 5, and a typical overlap of 95% the scanning speed, Eq. 6, is given by 22.5 mm/s. The scanning pitch between overlaping pulses is given by $2.25\,\mu$m. As discussed in Ref.[18] the scanning pitch is associated with the TFT pixel design and thus pixel size. According to that a small scanning pitch allows for higher pixel resolution. In comparison the typical excimer parameters $FWHM_{SA} \sim 500\,\mu$m and $f = 600\,\mathrm{Hz}$ Eq. 6 yield a scanning speed of $\sim 15\,\mathrm{mm/s}$ and a scanning pitch of $\sim 25\,\mu$m.

Based on our DPSSL technology the mentioned productivity can be even increased by increasing the number of laser sources. The latter comes along with a larger but still very small scanning pitch. Therefore, the SLA technology offers new opportunities to increase productivity and at the same time make higher resolution possible.

5. CONCLUSION

In this work we gave a brief insight on our DPSSL line beam technology with UV wavelength. We discussed the relevant beam shaping techniques and the possibilities that our technology offers. In this respect, the flexibility in terms of spatial and temporal beam shaping was mentioned and discussed in terms laser material processes that are relevant in the display industry, i.e. the laser lift off of flexible polyimide and the production of low temperature polysilicon. In both cases, it turns out that the DPSSL platform offers flexibility in beam shape and high throughput. In the context of LTPS we see an technological advantage in terms of temporal beam shaping. It opens new perspectives to finely control the process of melting, nucleation and crystal growth. Parameters like polycrystalline periodicity and surface roughness may be optimized by this additional control. The comparatively narrow short axis yields a very small scanning pitch which is potentially beneficial to reach higher display resolution. Furthermore the flexibility in polarization control can be used to optimize the process result. Apart from technological advantages the DPSSL platform offers high reliability and accordingly low maintenance costs. As compared to the excimer technology the process energy density is smaller, i.e. less average power is needed to obtain the same throughput.

APPENDIX A. LASER INDUCED PERIODIC SURFACE STRUCTURE

In the context of LTPS the light matter interaction can be reduced to a one-dimensional heat equation.[11] The reason is that the heat diffusion length $\xi \sim \sqrt{D\tau}$ is much smaller than lateral beam dimensions. Deviations to this one-dimensional behaviour may occur due to scattering effects from surface roughness.[14–16] To this end we have to consider the two-dimensional heat equation

$$\frac{\partial T}{\partial t} = \frac{\kappa}{\rho C_p}\left(\frac{\partial^2 T}{\partial z^2} - k_\perp^2 T\right) + \frac{\alpha}{\rho C_p} I(k_\perp, z, t). \tag{11}$$

Here ρ, C_p and κ are the density, the specific heat capacity and the thermal conductivity of silicon respectively. Furthermore, α is the absorption coefficient of silicon. The lateral spatial dimension is described by the spatial frequency $k_\perp$. In order to calculate the temperature distribution we first consider the case $k_\perp = 0$ and

$$I(k_\perp = 0, z, t) = \frac{F}{\tau}(1-R)\exp(-\alpha z)\theta(t)\theta(\tau - t), \tag{12}$$

where θ is the heaviside step-function, F is the fluence and τ is the pulse duration. This yields the homogeneous result[11]

$$T(k_\perp = 0, z = 0, \tau) = \frac{2F(1-R)}{\sqrt{\pi}\rho C_p \sqrt{D\tau}}, \tag{13}$$

which corresponds to Eq. 7 in the main text.

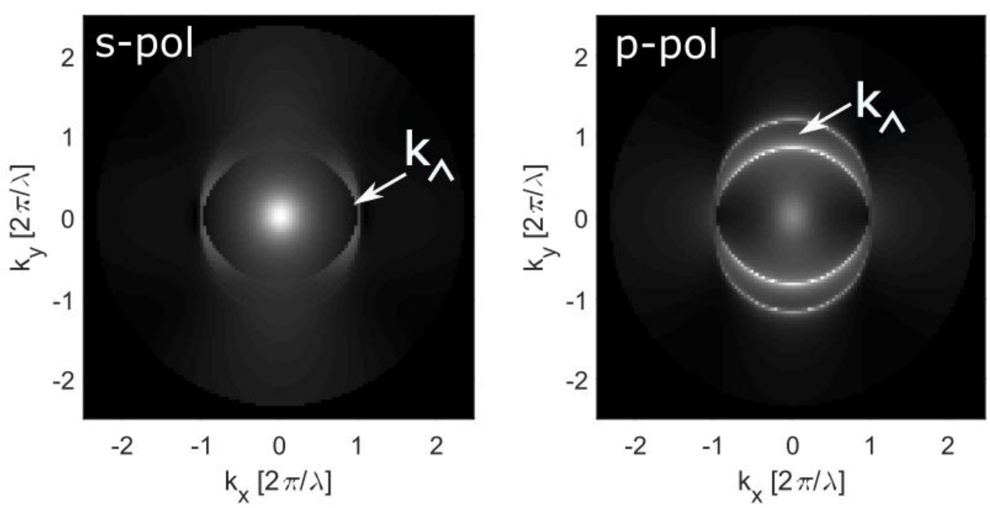

Figure 9. *Temperature Distribution* - The two-dimensional temperature distribution, Eq. 16, is shown for s- and p-polarized laser light respectively. The efficiency factor η for silicon was calculated as introduced in Ref.[15] The angle of incidence was chosen in the order of $\theta \sim 10°$. Here we used the material parameters mentioned in Ref.[16] as well as surface roughness parametrization as used in Refs.[14,15]

An arbitrary surface roughness can lead to an inhomogeneous absorption. In Ref.[15] it was shown that this coupling can be described in terms of an efficiency factor, i.e. $I \propto \eta(k_\perp, k_i)|b(k_\perp)|$. Here b is the spatial fourier transform of the surface roughness and η describes the interference by incoming and scattered waves. The latter depends on polarization, the permittivity of the material and on statistical parameters describing the surface roughness. Using the ansatz $T(k_\perp, z, t) = \hat{T}\exp(-Dk_\perp^2 t)$, where $D = \kappa/\rho C_p$, Eq. 14 yields the one-dimensional heat equation

$$\frac{\partial \hat{T}}{\partial t} = D\frac{\partial^2 \hat{T}}{\partial z^2} + \frac{\alpha}{\rho C_p} I(k_\perp, z, t)\exp(Dk_\perp^2 t). \tag{14}$$

For a semi-infinite half plane and for the boundary condition $\partial_z T|_{z=0} = 0$ the solution to this equation is given by

$$\hat{T} = \frac{\alpha}{\rho C_p}\int_0^\infty dz' \int_0^t dt' \exp(Dk_\perp^2(t-t'))G_N(z, z', t-t')I(k_\perp, z, t), \tag{15}$$

where $G_N(z, z', t') = \frac{1}{\sqrt{4\pi D t'}}\left[\exp(-(z-z')^2/4Dt') + \exp(-(z+z')^2/4Dt')\right]$. For $z = 0$ and in the limit of small diffusion length, $1/\alpha \ll \sqrt{D\tau}$, we obtain

$$T(k_\perp, z=0, t=\tau) = \frac{2F(1-R)}{\sqrt{\pi}\rho C_p\sqrt{D\tau}}\frac{\sqrt{\pi}}{2}\frac{\mathrm{erf}(\sqrt{D\tau}k_\perp)}{\sqrt{D}k_\perp}\eta(k_\perp, k_i)|b(k_\perp)|. \tag{16}$$

Using the parameters as suggested in Ref.[14] and the permittivity given in Ref.[16] we calculate the efficiency factor η as introduced in Ref.[15] The temperature distribution, Eq. 16, is shown in Fig. 9 for s- and p-polarized light. It shows pronounced features at $k_\perp = 0$ and $k_\perp = k_\Lambda$, the latter corresponding to a periodic pattern in real space with period Λ. Considering only these leading orders, $k_\perp = 0$ and $k_\perp = \pm|k_\Lambda|$, a fourier expansion of Eq. 16 to real space finally yields Eq. 9.

REFERENCES

1. R. F. Delmdahl and B. Fechner, "Large-area microprocessing with excimer lasers," *Applied Physics A* **101**, pp. 283–286, 2010.
2. R. Delmdahl, R. Paetzel, and J. Brune, "Large-area laser-lift-off processing in microelectronics," *Physics Procedia* **41**, pp. 241–248, 04 2013.
3. R. F. Delmdahl, M. Fricke, and B. Fechner, "Laser lift-off systems for flexible-display production," *Journal of Information Display* **15**, pp. 1 – 4, 2014.
4. C. Tillkorn, A. Heimes, D. Flamm, S. Dorer, T. Beck, J. Hellstern, F. Marschall, and C. Lingel, "Anamorphic beam shaping for efficient laser homogenization: methods and high power applications," **10518**, pp. 229 – 240, 2018.
5. F. Huneus, C. Lingel, T. Zeller, A. Heimes, C. Tillkorn, and K. Janami, "Compact line focus system for laser-based debonding of flexible electronic components," in *Laser-based Micro- and Nanoprocessing XIII*, U. Klotzbach, A. Watanabe, and R. Kling, eds., **10906**, pp. 42 – 48, International Society for Optics and Photonics, SPIE, 2019.
6. I. Choi, H. Y. Jeong, H. Shin, G. Kang, M. Byun, H. Kim, A. M. Chitu, J. S. Im, R. S. Ruoff, S.-Y. Choi, and K. J. Lee, "Laser-induced phase separation of silicon carbide," *Nature Communications* **7**, p. 13562, Nov 2016.
7. C. Berger, J.-F. Michaud, D. Chouteau, and D. Alquier, "Laser annealing simulations of metallisations deposited on 4h-sic," *Materials Science Forum, Trans Tech Publications* **963**, 2019.
8. F. Mazzamuto, S. Halty, H. Tanimura, and Y. Mori, "Low thermal budget ohmic contact formation by laser anneal," *Materials Science Forum* **858**, pp. 565–568, 05 2016.

9. R. Rupp, R. Kern, and R. Gerlach, "Laser backside contact annealing of sic power devices: A prerequisite for sic thin wafer technology," pp. 51–54, 2013.
10. J. Wager, "Tft technology:advancements and opportunities for improvement," *Information Display* , p. March/April, 2020.
11. S. D. Brotherton, "Polycrystalline silicon thin film transistors," **10**, pp. 721–738, jun 1995.
12. S. T. S. Oleg N. Prudnikov and B.-H. Cheong, "Laser pulse shape dependence of poly-si crystallization," *AIP Advances* **7**(125102), 2017.
13. P. C. van der Wilt and S. Passinger, "30-2: The crystallization monitor: Enabling accurate metrology of excimer-laser annealed si films," *SID Symposium Digest of Technical Papers* **48**(1), pp. 422–425, 2017.
14. J. Bonse and S. Gräf, "Maxwell meets marangoni—a review of theories on laser-induced periodic surface structures," *Laser & Photonics Reviews* **14**(10), p. 2000215, 2020.
15. H. M. van Driel, J. E. Sipe, and J. F. Young, "Laser-induced periodic surface structure on solids: A universal phenomenon," *Phys. Rev. Lett.* **49**, pp. 1955–1958, Dec 1982.
16. Z. Guosheng, P. M. Fauchet, and A. E. Siegman, "Growth of spontaneous periodic surface structures on solids during laser illumination," *Phys. Rev. B* **26**, pp. 5366–5381, Nov 1982.
17. R. Ishihara and M. Matsumura, "A novel double-pulse excimer-laser crystallization method of silicon thin-films," **34**, pp. 3976–3981, aug 1995.
18. J. Souk and et al., "Flat panel display manufacturing," *John Wiley and Sons* , 2018.